Available online at www.sciencedirect.com

ScienceDirect

Proceedings of the Combustion Institute 38 (2021) 6393–6401

Proceedings of the Combustion Institute

www.elsevier.com/locate/proci

Surrogate-based modeling for emulation of supercritical injector flow and combustion ☆

Xingjian Wang [a,*], Yu-Hung Chang [b], Yixing Li [b], Vigor Yang [b,*], Yu-Hsiang Su [c]

[a] *Mechanical and Civil Engineering, Florida Institute of Technology, Melbourne, FL, USA*
[b] *School of Aerospace Engineering, Georgia Institute of Technology, Atlanta, GA, USA*
[c] *Department of Aeronautics and Astronautics, National Cheng Kung University, Tainan, Taiwan*

Received 7 November 2019; accepted 22 June 2020
Available online 9 September 2020

Abstract

High-fidelity simulations play an increasingly important role in understanding fundamental turbulence-chemistry interactions and combustion dynamics in practical propulsion and power-generation systems. These simulations are, however, too computationally expensive and unwieldy for the purposes of design and optimization, given the large group of design parameters and wide design space. In this paper, we present an efficient surrogate-based modeling strategy to emulate spatiotemporal flows and combustion at supercritical pressures with accuracy similar to that of large-eddy simulations (LES). A common kernel-smoothed proper orthogonal decomposition (CKSPOD)-based surrogate model is developed, incorporating computer experiments, projection-based model reduction, kriging, and uncertainty quantification. The surrogate model (emulator) is carefully trained using a database drawn from a set of LES-based simulations that are conducted at designated sampling points in a given design space. A common Gram matrix is built using a Hadamard product to transform reduced spatial basis functions to remedy phase deviations among different design settings. Kriging is then used to obtain temporal spatial functions and associated coefficients for flowfield reconstruction at a new design setting.

The framework is examined with two case studies: an emulation of flow dynamics in a simplex swirl injector, and an emulation of mixing and combustion in a gas-centered liquid-swirl coaxial injector. The surrogate model not only faithfully captures the salient features of its LES counterpart, but also shortens the computation time dramatically, by up to five orders of magnitude. The developed surrogate model can be applied to a broad range of engineering systems and will provide support for future engineering innovation and design.

Keywords: Large eddy simulation (LES); Surrogate model; Supercritical; Common kernel-smoothed proper orthogonal decomposition (CKSPOD); Projection-based model reduction

☆ Choice of colloquium: GAS TURBINE AND ROCKET ENGINE COMBUSTION

* Corresponding authors.

E-mail addresses: wangx@fit.edu (X. Wang), vigor.yang@aerospace.gatech.edu (V. Yang).

https://doi.org/10.1016/j.proci.2020.06.303
1540-7489

1. Introduction

In this paper, we present an efficient modeling strategy to emulate spatiotemporally evolving flows and combustion at high pressures, a surrogate model of high-fidelity simulations for design survey. High-fidelity simulations, such as direct numerical simulation (DNS) and large eddy simulation (LES), play an increasingly important role in providing fundamental insight into turbulence-chemistry interactions and combustion dynamics in practical systems, but DNS and LES are computationally prohibitive, even with today's high-performance computing capabilities [1–3]. This makes system design optimization, which often involves multiple design parameters and a wide design space, a formidable task. As a result, most industrial companies still rely on low-fidelity models, such as Reynolds-averaged Navier-Stokes or analytical solutions, to meet practical turn-around times. To this end, we develop a surrogate model through emulation of LES-based simulations to predict the spatiotemporal flowfield. The model not only faithfully captures salient features of its LES counterpart, but also shortens the computation time dramatically, typically by up to five orders of magnitude.

Surrogate models, also known as metamodels, have frequently been used in design and analysis of computer experiments over the last three decades [4]. Surrogate models are constructed based on data drawn from computer experiments, and provide fast approximations of the objectives and constraints at new design points, thereby making design and optimization studies feasible and economical [5]. Various statistical prediction approaches have been proposed to build effective surrogate models, including the polynomial response surface model, moving least squares, radial basis functions, support vector regression, and kriging. Surrogate-based methods have been reviewed comprehensively several times, including for aerospace system design [6,7] and multidisciplinary design optimization [8].

Most existing modeling techniques, however, focus on single or multiple outputs, and surrogate models with functional responses have been much less documented in literature. Kriging, as one of the most promising techniques due to its interpolating property, is appealing for use in modeling output of computer experiments [5,9]. But it encounters a critical issue – the curse of dimensionality – when dealing with high-dimensional data with functional outputs [10]. For the prediction of spatiotemporal flowfields in combustion engines, a kriging process needs to handle flow information on millions of computational cells and at thousands of time steps at different design settings [11]. The resultant data matrix is too large to process using existing models. Data-reduction methods are thus needed before the kriging technique can be implemented.

Many reduced-basis models have been used to overcome the dimensionality of datasets, such as wavelet decomposition [12], functional linear models [13], and proper orthogonal decomposition (POD) [14]. The models that project the data from a high-dimensional space into a subspace with a reduced set of basis functions are called projection-based reduced-order models (ROMs). The operators of the reduced model are constructed by projecting the equations of the full model onto a reduced space. Projection-based ROMs are fairly intrusive, which means that full-model operators need to be available explicitly or implicitly to obtain ROMs at given design settings. In the present paper, we approach projection-based ROMs in a non-intrusive way. Instead of focusing on operators of equations, we develop reduced POD basis functions using a data-driven approach.

POD has been widely used in dimension reduction for large-scale dynamical systems [15]; it produces an optimal set of orthonormal basis functions (POD modes) through singular value decomposition, and minimizes the least square errors of data reconstruction. These POD modes represent the most dominant flow dynamics in the flowfield. A novel surrogate modeling technique, common kernel-smoothed POD (CKSPOD) is proposed and implemented here. CKSPOD builds a common Gram matrix using a Hadamard product, and efficiently predicts the complex flowfield over a broad range of operating conditions and geometric parameters. The CKSPOD-based surrogate model is considered to be the crucial part of the data-driven emulation framework for design and optimization. Section 2 provides a detailed description of the CKSPOD-based surrogate methodology. In Section 3, the framework is applied and examined through two case studies, a simplex swirl injector and a gas-centered liquid-swirl coaxial injector. Section 4 concludes this work.

2. Surrogate-based modeling framework

Surrogate-based modeling is the core of the surrogate-based design and optimization framework. To enable this framework, a sampling plan (or design space) first must be configured, based on preliminary experiments and prior knowledge from analytical solutions. A group of design parameters and associated value ranges are included in the design space. The number of design settings is then determined using design of experiments, such as sliced Latin-hypercube design (SLHD) [16]. Next, LES-based simulations are performed at each design setting, and the resultant simulation data are collected for the training of the surrogate model. The detailed formulation of the proposed CKSPOD-based surrogate model is provided in the next section.

2.1. Projection-based model reduction

For a sampling plan with p design parameters, the number of design settings for training is q, according to design of experiment. The objective of the present work is to emulate the spatiotemporal flowfield at unobserved design settings, and the training data must accordingly include spatially distributed flow information in different snapshots.

The POD-type projection-based model reduction is implemented to build the emulator. The POD analysis is performed by the method of snapshots. We use $f(\boldsymbol{x}, t)$ to denote the variable of interest at location $\boldsymbol{x}$ and time t. All data at an observed design setting i ($i = 1, \ldots, q$) can be represented by a snapshot matrix, $\boldsymbol{X}_i \in \mathbb{R}^{n\times m}$, where n is the total number of discretized cells and m the number of temporal snapshots. The former is much larger than the latter for the present applications, $n \gg m$, which is true for most high-fidelity simulations.

The matrix $\boldsymbol{X}_i$ can be uniquely factorized through singular value decomposition (SVD),

$$\boldsymbol{X}_i = \boldsymbol{U}_i \boldsymbol{\Lambda}_i \boldsymbol{V}_i^T, \quad i = 1, \cdots, q, \tag{1}$$

where $\boldsymbol{U}_i$ is an $n \times n$ orthonormal matrix spanning $\boldsymbol{X}_i$'s column space $\mathrm{im}(\boldsymbol{X}_i)$, $\boldsymbol{\Lambda}_i$ an $n \times m$ diagonal matrix of singular values, and $\boldsymbol{V}_i$ an $m \times m$ orthonormal matrix spanning $\boldsymbol{X}_i$'s row space $\mathrm{im}(\boldsymbol{X}_i^T)$. The singular values $\sigma_1 \geq \sigma_2 \geq \ldots \geq \sigma_l \geq 0$, and $l \leq m \ll n$. In our case studies, the snapshot matrix $\boldsymbol{X}_i$ tends to be full rank with $l = m$. $\boldsymbol{U}_i$and $\boldsymbol{V}_i$ are related to the eigenvectors of $\boldsymbol{X}_i\boldsymbol{X}_i^T$ and $\boldsymbol{X}_i^T\boldsymbol{X}_i$, respectively. Denote the Gram matrix $\boldsymbol{X}_i^T\boldsymbol{X}_i$ as $\boldsymbol{C}_i$, and the eigenvectors of $\boldsymbol{C}_i$ make up the colums of $\boldsymbol{V}_i(\boldsymbol{C}_i = \boldsymbol{V}_i\boldsymbol{L}_i\boldsymbol{V}_i^T)$, where $\boldsymbol{L}_i = \boldsymbol{\Lambda}_i^T\boldsymbol{\Lambda}_i \in \mathbb{R}^{m\times m}$ is the diagonal matrix of eigenvalues of $\boldsymbol{C}_i$). Following this way, $\boldsymbol{C}_i$ becomes a much smaller matrix and its eigen-decomposition is significantly faster than that of $\boldsymbol{X}_i\boldsymbol{X}_i^T$. The eigenvectors $\boldsymbol{V}_i$ represents the POD temporal coefficients. The corresponding spatial modes are deduced as $\boldsymbol{\Phi}_i = \boldsymbol{X}_i\boldsymbol{V}_i \in \mathbb{R}^{n\times m}$. The reduced POD coefficients of dimension r, $\boldsymbol{V}_i^r = [\boldsymbol{v}_i^1, \boldsymbol{v}_i^2, \ldots, \boldsymbol{v}_i^r] \in \mathbb{R}^{m\times r}$, are defined as the first r column vectors of the orthonormal matrix of $\boldsymbol{V}_i$. This selection of $\boldsymbol{V}_i^r$ ensures the minimization of the least squares error of snapshot reconstruction and gives the reduced spatial modes matrix as $\boldsymbol{\Phi}_i = \boldsymbol{X}_i\boldsymbol{V}_i^r \in \mathbb{R}^{n\times r}$. Such reduction in modes and coefficients alleviates the storage memory load significantly and further accelerates the establishment of the surrogate model.

The kernel-smoothed POD (KSPOD) technique [17] was previously proposed to estimate spatial functions at unobserved design settings with the incorporation of the POD spatial modes at every sampling point using kriging. However, KSPOD encounters difficulty when the POD modes at different sampling points deviate or have phase shift, as manifested by the element signs in the POD mode matrix. To remedy this issue, we develop a new approach, called CKSPOD, which transfers the POD modes at different sampling points by constructing a common Gram matrix.

2.2. Common Gram matrix

In CKSPOD, a common Gram matrix $\mathbb{C}$, which synthesizes the temporal information on all training data, is constructed as the Hadamard product of the Gram matrices at every observed setting. A Hadamard operator, denoted as $\circ$, is the element-to-element multiplication of two matrices of similar dimension, for example,

$$\begin{bmatrix} a_{11} & a_{12} \\ a_{21} & a_{22} \end{bmatrix} \circ \begin{bmatrix} b_{11} & b_{12} \\ b_{21} & b_{22} \end{bmatrix} = \begin{bmatrix} a_{11}b_{11} & a_{12}b_{12} \\ a_{21}b_{21} & a_{22}b_{22} \end{bmatrix}$$

Following this definition, the common Gram matrix is expressed as,

$$\mathbb{C} = \boldsymbol{C}_1 \circ \boldsymbol{C}_2 \circ \ldots \circ \boldsymbol{C}_q = \mathbb{V}\mathbb{L}\mathbb{V}^T, \tag{2}$$

where $\mathbb{V}$ is the column matrix of eigenvectors of $\mathbb{C} \in \mathbb{R}^{m\times m}$, and $\mathbb{L}$ is the corresponding diagonal matrix. Every Gram matrix ($\boldsymbol{C}_i$) contains the temporal dynamics of the flowfield at the corresponding sampling point, and the common Gram matrix synthesizes all these temporal dynamics through element-wise multiplication. An inherent assumption applied in Eq. (2) is that the number of snapshots (m) collected for each design setting is identical. This ensures the same dimension for all Gram matrices, as required for the Hadamard product. If the computational cells for various design settings are different, a common grid system is required for the projection of data information from the original cells.

Earlier KSPOD work [17] revealed that the direct incorporation of the original POD spatial modes at different sampling points may induce the cancellation effect in mode shape. The temporal coefficient matrix $\mathbb{V}$ that incorporates the dynamic information of all training data is used to transform the original spatial modes, a method to align the modes at different design settings. The transferred spatial modes of the design setting i, $\boldsymbol{\Phi}'_i$ are represented as,

$$\boldsymbol{\Phi}'_i = \boldsymbol{X}_i\mathbb{V} = \boldsymbol{X}_i\mathbb{C}\mathbb{V}\mathbb{L}^{-1}. \tag{3}$$

Note that mode reduction is also performed here with the first r columns included for data reconstruction and the superscript r is skipped for brevity. With the commutative property for the Hadamard product, substituting Eq. (2) into Eq. (3) yields the connection between the transferred spatial modes and original POD modes,

$$\boldsymbol{\Phi}'_i = \boldsymbol{X}_i\boldsymbol{V}_i\mathcal{T} = \boldsymbol{\Phi}_i\mathcal{T} \tag{4}$$

Here the matrix $\mathcal{T}$ is defined as $\mathcal{T} = [\boldsymbol{L}_i\boldsymbol{V}_i^T \circ (\Pi_{\substack{j=1\\ j\neq i}}^{q} \boldsymbol{C}_j)]\mathbb{V}\mathbb{L}^{-1}$, and $\mathcal{T}$ can be considered as a CKSPOD transfer matrix, which converts the original POD modes to the spatial functions at each design setting. To utilize these spatial

functions properly with kriging-based weights for new design settings, a normalization process is performed on column vectors ($\boldsymbol{\phi}_i'^k$, $k = 1, \ldots, r$) of $\boldsymbol{\Phi}'_i$,

$$\tilde{\boldsymbol{\phi}}_i^k = \boldsymbol{\phi}_i'^k / \left\| \boldsymbol{\phi}_i'^k \right\|_2. \tag{5}$$

Accordingly, the matrix of the transferred temporal coefficients ($\tilde{\boldsymbol{B}}_i$) absorbs the normalization factor. Once the matrices of the transferred spatial functions and time-varying coefficients are deduced, kriging is implemented to develop the basis functions and coefficients for a new design setting in the design space.

2.3. Kriging

Kriging, a widely used surrogate-based modeling approach, models an unknown, deterministic function as a realization of a stochastic process [5]. The kriging predictor is a best, unbiased predictor that is linear in sample responses and can be nonlinear in responses' coefficients. In the present fluid flow problem, the sample responses include the transferred spatial functions and temporal coefficients. For a set of design settings $\{\boldsymbol{d}_i \in R^p\}_{i=1}^q$, the observed functions of interest are weighting parameters of transferred spatial functions and corresponding temporal coefficients at sampling points. Based on the training dataset of a $\boldsymbol{d}_i - \boldsymbol{y}_i$ pair, with a new input $\boldsymbol{d}_{new}$, kriging predicts the corresponding response $\boldsymbol{y}_{new}$. The mathematical formula of kriging in terms of prediction $\boldsymbol{y}_{new}$ is given by:

$$\hat{\boldsymbol{y}}_{new} = \hat{\boldsymbol{\mu}} + \boldsymbol{r}_{\boldsymbol{new}}^T \boldsymbol{R}^{-1}\left(\boldsymbol{y} - \mathbf{1}_{\boldsymbol{q}}\hat{\mu}\right) \tag{6}$$

where $\hat{\boldsymbol{\mu}} = \mathbf{1}_{\boldsymbol{q}}^T \boldsymbol{R}^{-1}\boldsymbol{y} / \mathbf{1}_{\boldsymbol{q}}^T \boldsymbol{R}^{-1}\mathbf{1}_{\boldsymbol{q}}$ is the maximum likelihood estimate of $\boldsymbol{\mu}$. $\mathbf{1}_{\boldsymbol{q}}$ is q–vector of 1′s, and $\boldsymbol{R}$ is a $q \times q$ matrix of a re-parameterized squared-exponential correlation function whose (i, j)-th entry is $r(\boldsymbol{d}_i, \boldsymbol{d}_j) = \exp\{-\sum_{k=1}^p \theta_k (d_{kj} - d_{ki})^2\}$, a Gaussian-like kernel with scaling parameter $\theta_k = -4 \log d_k$. This allows for a more numerically stable optimization of maximum likelihood estimators [18]. The correlation function measure is a weighted-distance formula. When the distance between the sampling points in the input space is small, the correlation approaches 1. Likewise, when the distance is large, the correlation approaches 0. $\boldsymbol{r}_{\boldsymbol{new}}$ is a q-vector whose i_{th} entry is the correlation function between the unobserved point and sampling points $\boldsymbol{r}(\boldsymbol{d}_{new}, \boldsymbol{d}_i)$.

Replacing $\boldsymbol{y}$ in Eq. (6) by the column vectors of $\tilde{\boldsymbol{B}}_i$ ($\tilde{\boldsymbol{\beta}}_i^k$, $k = 1, \cdots, r$), the predicted time-varying coefficients at unobserved design setting $\hat{\boldsymbol{B}}_{new}(\hat{\boldsymbol{\beta}}_{new}^k, k = 1, \cdots, r)$ can be obtained. The spatial basis functions are calculated in a slightly different way. Kriging is used to predict the weight of each spatial function at observed points on the spatial function at the new design setting. The observations $\boldsymbol{y}$ are now taken to be the orthonormal vector $\boldsymbol{e}_i$, where $\boldsymbol{e}_i$ is a q-vector with 1 in its i-th element and 0 elsewhere. Intuitively, this quantifies the fact that the spatial mode information extracted in the i-th design setting corresponds to only that setting and not the other $q - 1$ settings. The resulting predictor in Eq. (6) can be viewed as the predicted weight for that particular spatial mode at the new design setting $\boldsymbol{d}_{new}$, denoted as $\hat{w}_{new,i}$ This procedure is repeated for each of the q unit vectors $(\boldsymbol{e}_i)_{i=1}^q$, from which the q weighting parameters $(\hat{w}_{new,i})_{i=1}^q$ can be obtained. The weighting parameters are normalized to ensure that their summation is equal to unity.

The weighting parameters are subsequently used to predict the spatial functions at the new design setting through a weighted average of the transferred POD modes at the observed design settings, and they are expressed as,

$$\hat{\boldsymbol{\phi}}^k(\boldsymbol{d}_{new}, \boldsymbol{x}) = \sum_{i=1}^{q} \hat{\boldsymbol{w}}_{\boldsymbol{new},\ i} \tilde{\boldsymbol{\phi}}_{\boldsymbol{i}}^k \tag{7}$$

Instead of applying universal POD modes in CPOD [19], we implement weighting functions to transferred POD spatial modes with a common Gram matrix and a kernel-smoothed algorithm, referred to as common kernel-smoothed POD (CK-SPOD). Combining time-varying coefficients and spatial functions obtained using Eqs. (6),(7), the predicted spatiotemporal flowfield at a new design setting is

$$\hat{\boldsymbol{X}}(\boldsymbol{d}_{new}, \boldsymbol{x}, \boldsymbol{t}) = \sum_{k=1}^{r} \hat{\boldsymbol{\phi}}^k \left(\hat{\boldsymbol{\beta}}^k\right)^{\boldsymbol{T}} = \hat{\boldsymbol{\Phi}}\hat{\boldsymbol{B}}^{\boldsymbol{T}}, \tag{8}$$

with $\hat{\boldsymbol{X}}(\boldsymbol{d}_{new}, \boldsymbol{x}, t) \in \mathbb{R}^{n \times m}$. Eq. (8) emulates the spatiotemporal flowfield at a new design setting in a physics-based data-driven way without performing a new high-fidelity simulation. A key advantage of kriging is that it does not just predict the spatiotemporal flowfield at unobserved design settings, but it also allows quantification of the uncertainty associated with the prediction.

2.4. Uncertainty quantification (UQ)

In this work, we assume that the database drawn from high-fidelity LES simulations is reliable and accurate, and the uncertainty of statistical prediction primarily comes from model reduction and the kriging process. Previous work [18] has shown that invoking the conditional distribution of the multivariate normal distribution, the kriging-predicted time-varying coefficients at a new design setting follow a Gaussian distribution, $\tilde{\boldsymbol{\beta}}(\boldsymbol{d}_{new}) | \{\tilde{\boldsymbol{\beta}}(\boldsymbol{d}_i)\}_{i=1}^q \sim N(\hat{\boldsymbol{\beta}}, \hat{\boldsymbol{\Sigma}})$. Here the kriging predictor $\hat{\boldsymbol{\beta}}$ for $\tilde{\boldsymbol{\beta}}(\boldsymbol{d}_{new})$ has been defined in Eq. (6), and its corresponding variance is given by,

$$\hat{\boldsymbol{\Sigma}} = \left(1 - \mathbf{r}_{\boldsymbol{new}}^T \boldsymbol{R}^{-1} \mathbf{r}_{\tau,\boldsymbol{new}}\right) \boldsymbol{T} \tag{9}$$

where $\boldsymbol{I}_{\boldsymbol{m}}$, $\mathbf{1}_q$ and $\boldsymbol{T}$ are the $m \times m$ identity matrix, 1-vector of q elements, and $r \times r$ covariance matrix, respectively.

Similarly, the variance associated with the weights of the predicted spatial functions during kriging at a new design setting can be also represented by Eq. (9), but with $\boldsymbol{T}$ as identity matrix. The UQ of the final prediction using Eq. (8) can be calculated through the propagation of UQs of time-varying coefficients and spatial functions weights. The spatiotemporal variance is expressed as,

$$\begin{aligned}&\mathbb{V}\{\boldsymbol{X}(\boldsymbol{x},t;\boldsymbol{d}_{new})\}\big|\{\boldsymbol{X}(\boldsymbol{x},t;\boldsymbol{d}_i)\}_{i=1}^{q}\\&=\sum_{k=1}^{r}\mathbb{V}\left\{\tilde{\boldsymbol{\beta}}^{\boldsymbol{k}}(\boldsymbol{d}_{new})\Big|\left\{\tilde{\boldsymbol{\beta}}(\boldsymbol{d}_i)\right\}_{i=1}^{q}\right\}\\&\sum_{i=1}^{q}\mathbb{V}\left\{w(d_{new})\big|\{w(d_i)\}_{i=1}^{q}\right\}\left\{\tilde{\boldsymbol{\phi}}_i^{k}(\mathbf{x})\right\}^2\end{aligned}\tag{10}$$

3. Case study

In the present study, we examine two representative cases of swirl-related flows to validate the surrogate-based modeling framework, since swirling flows have been widely used to stabilize combustion in aerospace propulsion and combustion [20]. The first validation case is to emulate flow dynamics in a simplex swirl injector, while the second case is to emulate the mixing and combustion flowfield in a gas-centered liquid swirl injector. The operating pressure of both cases is set as supercritical for two reasons. First, this pressure condition is encountered in many advanced propulsion engines, such as liquid rockets and gas turbines. Second, higher pressure implies higher Reynolds number and a wider range of turbulent scales to resolve, leading to a computationally more challenging task [11,21]. The theoretical and numerical framework for LES-based high-fidelity simulations of supercritical fluid flows and combustion has been detailed in previous publications [11,21] and is not elaborated here.

3.1. Simplex swirl injector

A schematic of a simplex swirl injector is shown in Fig. 1. Liquid oxygen (LOX) at 120 K is injected tangentially into a supercritical oxygen environment at 300 K and 10 MPa through discrete orifices, which are simplified into a single radial slit for cylindrical sector configuration with periodic boundary condition specified in the azimuthal direction. The slit width is correlated to the orifice diameter (D_{in}) through mass conservation. An earlier parametric study [19] has identified three design parameters that are important to injector performance: inlet slit width (δ), inlet injection angle (θ), and distance between inlet slit and injector head-end (ΔL). The design ranges of δ and θ are selected based on the desired performance metrics (spreading angle and film thickness), according to the empirical model. δ ranges from 0.27 mm to 1.53 mm, θ ranges from 35.0° to 62.2°, and ΔL is varied from 0.85 mm to 3.4 mm. With the selected design parameters and associated ranges, the SLHD is then implemented to generate 30 design settings based on the $10p$ rule-of-thumb. Another 2 design settings (with values of (1.20 mm, 41.97°, 0.90 mm) and (0.49 mm, 57.12°, 2.88 mm), respectively) were selected for validation purposes. LES-based simulations were performed at all (30+2) design settings, producing a large spatiotemporal database for the training of the CKSPOD-based surrogate model. For every design setting, 1000 flow snapshots were collected in the time period of 10 ms after the flow reaches a statistically stationary state.

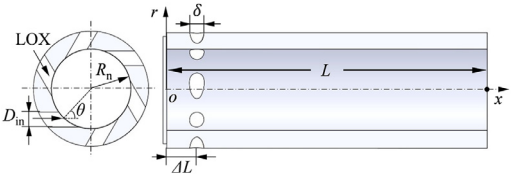

Fig. 1. Schematic of swirl injector.

3.1.1. CKSPOD prediction

Figure 2 shows a comparison of instantaneous density distributions between LES and CKSPOD in Cases 1 and 2. The two validation cases are selected to represent two distinct flow patterns and

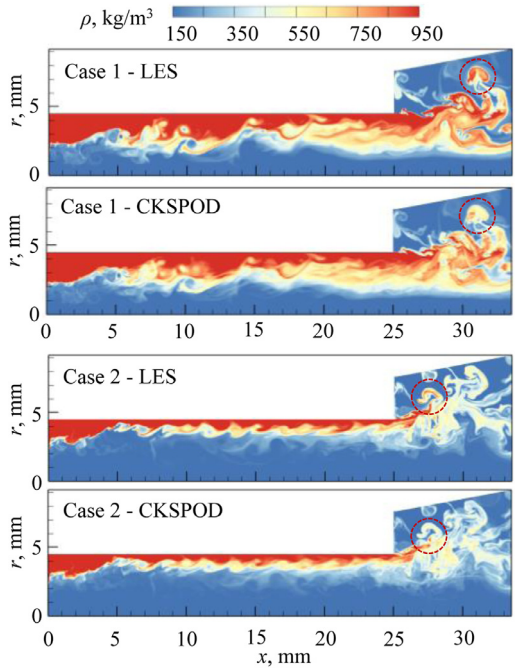

Fig. 2. Instantaneous density distributions: LES and CKSPOD in Cases 1 and 2.

dynamics in a simplex swirl injector. The swirl-induced centrifugal force drives the LOX film to flow along the injector surface and a low-density gas-like core forms in the center region. In this supercritical pressure environment, the density varies smoothly in the radial direction from a liquid state near the wall to a supercritical (gas-like) state in the core region. The interfacial region shows significantly different vortical structures in different cases. Detailed discussion on LOX swirling flow dynamics can be found in Ref. [22].

Liquid film thickness and spreading angle are two important factors that determine mixing efficiency and flow dynamics. As shown in LES results, Case 1 with smaller θ results in thicker liquid film thickness and smaller spreading angle at the injector exit than Case 2. In both validation cases, the overall prediction by CKSPOD shows excellent agreement with simulation by LES. The ligaments and wrinkled structured on the surface of the liquid film in the injector are well captured in Case 1, and a row of vortex rolling motions is accurately predicted in Case 2. Downstream of the injector, the spreading of the liquid film and the growth of vortical structures along the liquid film are predicted very well. Although the CKSPOD prediction of dynamical structures in the flowfield is promising, however, the numerical values of density in the circled regions are underestimated in both cases. It is possible that adding more sampling points near the validation cases could improve the prediction.

3.1.2. Uncertainty quantification

Table 1 shows a comparison of averaged film thickness and spreading angle for LES-based simulation and CKSPOD-based emulation in both cases. Note that these values were taken from the averaging of 1000 snapshots of simulations and emulations at the injector exit. It is seen that the predicted film thickness and spreading angle have relative errors less than 1% in Case 1 and less than 0.1% in Case 2. Further analysis was conducted on the axial distribution of the liquid film surface, and local relative errors are less than 3% (not shown here). The magnitude of the relative errors is similar, implying the high fidelity of the present CKSPOD-based emulator.

The quantification of the prediction uncertainty is demonstrated using a derived flow property, turbulent kinetic energy (TKE). Figure 3 shows

Table 1
Prediction of averaged film thickness and spreading angle.

	Case number	1	2
film thickness	LES	0.637	0.471
	CKSPOD	0.640	0.471
spreading angle	LES	52.566	57.778
	CKSPOD	52.657	57.750

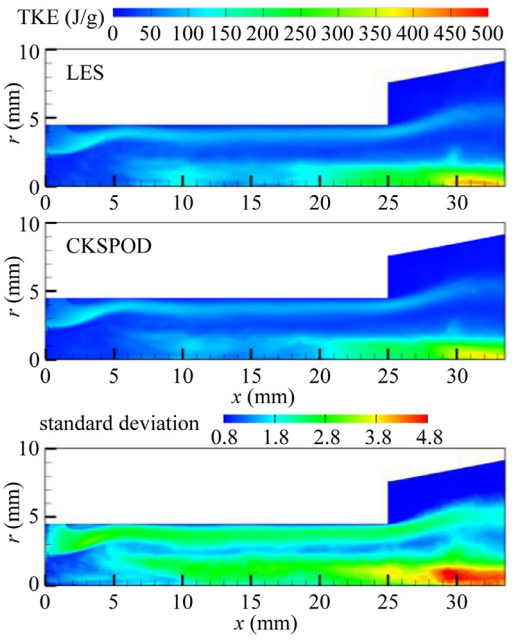

Fig. 3. Spatial distributions of time-averaged TKE from LES (top) and CKSPOD (middle) and associated standard deviation (bottom) in Case 1.

time-averaged spatial distributions of TKE from LES and CKSPOD, along with the standard deviation of the CKSPOD result in Case 1. In LES, high TKE values occur along the surface of the liquid film and near the center region of the injector exit; this is caused by strong shear-layer dynamics and flow recirculation in these regions [22]. The CKSPOD prediction bears close resemblance to the LES TKE distribution with major features captured. Further evidence can be seen from the standard deviation for CKSPOD prediction, which was calculated according to the variance defined in Eq. (10). A smaller standard deviation denotes a lower uncertainty of prediction. The regions with most uncertain predictions coincide with the regions with most intense dynamics. The maximum of standard deviation is close to 5, compared to the maximum TKE of around 500.

3.1.3. Computation time

The motivation for developing a surrogate-based model is to reduce the prohibitive computation time required for high-fidelity simulations for design purposes. For the present axisymmetric LES-based simulations, the computation time at different design settings varies from 10 to 14 days on around 320 CPUs. In comparison, the time required to build the surrogate model is about 73 min on 10 CPUs, and the time for emulating a new case using the developed surrogate model is only 7 min on 5 CPUs. Therefore, the time saving of emulation

is about 5 orders of magnitude, compared to simulation.

3.2. Gas-centered liquid-swirl coaxial (GCLSC) injector

Mixing and combustion of gaseous oxygen (GOX) and kerosene at supercritical pressure (p=25.3 MPa) offers a second representative case for emulation. The flow dynamics and combustion of GCLSC injectors have been systematically investigated in previous work [23-25]. Figure 4 shows a schematic of the region of interest for emulation of mixing and combustion dynamics. Note that this region only covers a part of a GCLSC injector, where important physics, including fuel-oxidizer mixing and flame anchoring, are involved. (The region could easily be extended if needed.)

Yang and colleagues [23,24] have identified the recess length (L_r) as one of the most important design parameters for mixing and combustion efficiencies. For demonstration purposes, therefore, recess length is regarded as the single design parameter for the surrogate model. The theoretical range of L_r is from 0 (no recess) to L_f (fully recessed). A total of 12 design settings were produced in the range of $0 < L_r < L_f$, where L_f=16 mm. The cases with no recess and full recess are excluded here as outliers, because earlier studies [23,24] have found that those two cases show significantly different flow and flame dynamics from other cases. One setting with L_r=8.75 mm is selected as the validation case, and the remaining 11 design settings are training cases. Since only one design parameter is involved for this case study, weighting parameters are calculated differently from the previous case. An inverse distance weighting is applied, $\hat{w}_i(\boldsymbol{d}_{new}, \boldsymbol{d}_i) = 1/|\boldsymbol{d}_{new} - \boldsymbol{d}_i|^2$.

The training database includes 1000 flow snapshots in a time span of 10 ms for the pure-mixing case and 400 flow snapshots in 4 ms for the combustion case. A special treatment of the irregular grid system is needed before model reduction and kriging. With the variation of recess length, the computational grid in Zone 1 changes, since the recess region next to the GOX post tip that is a grid section in cases with longer recess is represented as a part of the post in cases with shorter recess. To this end, we establish a common grid system for all design settings, into which all simulation data are projected. The data in Zone 1 is divided into 3 subzones (GOX post, recess, fuel passage), and each subzone is projected into the respective subzone in the common grid system. This technique is particularly useful with design spaces involving varying geometries or different grid systems [18,19].

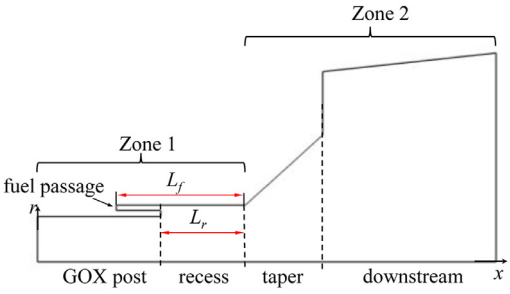

Fig. 4. Schematic region of a GCLSC injector for emulation.

3.2.1. CKSPOD prediction

Figure 5 shows instantaneous density distributions from LES and CKSPOD in the pure-mixing case. The results predicted by CKSPOD capture the primary characteristics of the mixing field, such as the overall shape of the central GOX core, the kerosene film development along the fuel passage and injector surface, and large coherent structures in the mixing layer. A detailed discussion on model performance and uncertainty quantification will be presented in a future paper.

Figure 6 shows a comparison of instantaneous temperature distributions in the combustion case. The CKSPOD-based surrogate model successfully predicts the flame anchoring near the GOX post tip. The wrinkled flame shape is roughly captured in the recess and taper regions. The prediction accuracy appears lower than that in pure-mixing case, but this could be improved by including more snapshots at all sampling points. Note that LES-based simulation is extremely challenging in the combustion case at supercritical pressure, in terms of computational time and numerical convergence.

To further quantify accuracy, Figure 7 shows a comparison of contour lines of the averaged mixture-fraction field in the combustion case. The contour line of 0.225 represents the stoichiometric mixing line, which is often used to denote the flame surface in flamelet-based combustion models. The

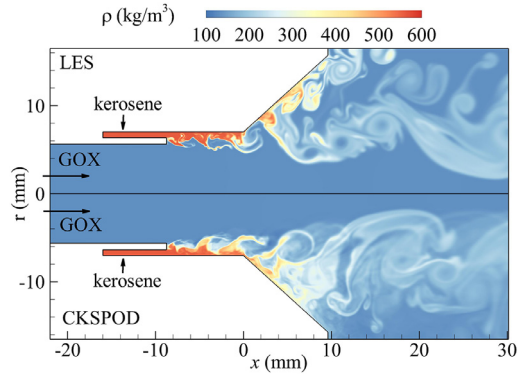

Fig. 5. Instantaneous density distributions from LES (top) and CKSPOD (bottom) in pure-mixing case.

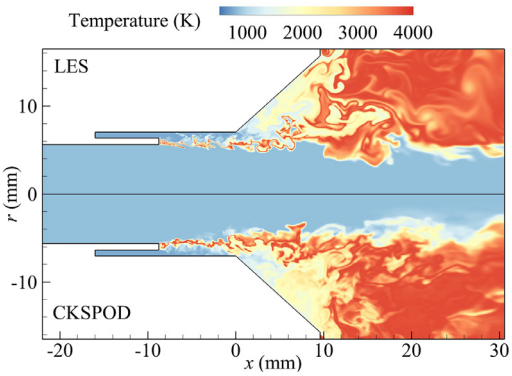

Fig. 6. Instantaneous temperature distributions for LES (top) and CKSPOD (bottom) in combustion case.

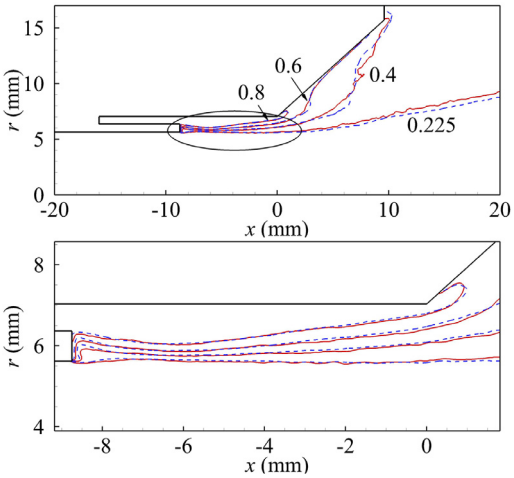

Fig. 7. Contour lines of averaged mixture-fraction field for LES (solid lines) and CKSPOD (dashed lines): overview (top) and zoomed-in view (bottom).

CKSPOD-predicted contour lines match the LES results well, except in the upper region of the taper, where the current 400 snapshots in 4 ms is probably insufficient to obtain an averaged distribution. Nonetheless, the zoomed-in view in the recess region shows excellent agreement between CKSPOD and LES at all contour levels. This demonstrates the accuracy of both the common grid system and the CKSPOD-based emulation.

3.2.2. Computation time

For cold flows, the LES-based simulations require approximately 100,000 CPU hours for a time span of 10 ms (1000 snapshots), as compared to 12 CPU hours for the training of the surrogate model and 60 s of CPU time for each snapshot of prediction using the CKSPOD-based model. The CKSPOD-based model is roughly 6000 times faster than LES-based simulations. The speedup is more significant for reacting flows for the same time span, due to the fact that LES-based simulations require much smaller time-marching steps in numerical calculations.

4. Conclusion

A novel surrogate model, common kernel-smoothed proper orthogonal decomposition (CKSPOD), is proposed for emulation of large eddy simulations of turbulent flows and combustion at supercritical pressure. The CKSPOD-based framework is multi-disciplinary, incorporating high-fidelity simulations (computer experiments), design of experiment, projection-based model reduction, kriging, and uncertainty quantification (UQ). It leverages the implementation of the Hadamard product to build a common Gram matrix that is used to transfer and align POD spatial modes at training design settings. The prediction of the spatiotemporal flowfield at a new design setting is fulfilled through data reconstruction of spatial modes and coefficients obtained via kriging. The UQ associated with kriging is detailed. Two validation cases are presented; one is to emulate the flow dynamics of a simplex swirl injector, and the other is to emulate the mixing and combustion of a gas-centered liquid-swirl coaxial injector (GCLSC). In the simplex swirl injector case, excellent agreement is achieved between the emulated results and LES results, in terms of instantaneous flow distribution, large-coherent structures, and injector performance metrics. Large uncertainty occurs in regions of shear layers and center flow recirculation. In the GCLSC case, the overall predictions of mixing and combustion are promising. The location of flame anchoring is captured, and the contour lines of the averaged mixture fraction field are accurately predicted. Accuracy could be further improved by including more snapshots in the training database.

Declaration of Competing Interest

None.

Acknowledgments

The authors would like to thank Dr. C. F. Jeff Wu, Dr. Simon Mak, and Dr. Chih-Li Sung for discussions on emulation.

References

[1] T. Poinsot, S. Candel, A. Trouvé, *Prog. Energy Combust. Sci.* 21 (1995) 531–576.
[2] J.H. Chen, *Proc. Combust. Inst.* 33 (2011) 99–123.
[3] H. Pitsch, *Annu. Rev. Fluid Mech.* 38 (2006) 453–482.

[4] T.W. Simpson, J.D. Poplinski, P.N. Koch, J.K. Allen, *Eng. Comput.* 17 (2001) 129–150.
[5] J. Sacks, W.J. Welch, T.J. Mitchell, H.P. Wynn, *Stat. Sci.* 4 (1989) 409–423.
[6] N.V. Queipo, R.T. Haftka, W. Shyy, T. Goel, R. Vaidyanathan, P.K. Tucker, *Prog. Aerosp. Sci.* 41 (2005) 1–28.
[7] A.I.J. Forrester, A.J. Keane, *Prog. Aerosp. Sci.* 45 (2009) 50–79.
[8] T. Simpson, V. Toropov, V. Balabanov, F. Viana, in: Proceedings of the 12th AIAA/ISSMO multidisciplinary analysis and optimization conference, 2008 2AIAA Paper No. 2008-5802.
[9] D.R. Jones, M. Schonlau, W.J. Welch, *Journal of Global optimization* 13 (1998) 455–492.
[10] Y. Hung, V.R. Joseph, S.N. Melkote, *Technometrics* 57 (2015) 35–44.
[11] X. Wang, H. Huo, U. Unnikrishnan, V. Yang, *Combust. Flame* 195 (2018) 203–215.
[12] M.J. Bayarri, J.O. Berger, R. Paulo, J. Sacks, J.A. Cafeo, J. Cavendish, C.-H. Lin, J. Tu, *Technometrics* 49 (2007) 138–154.
[13] J.O. Ramsay, in: Functional Data Analysis, Springer Science+Business Media, Inc., 2004, p. 217.
[14] P. Benner, S. Gugercin, K. Willcox, *SIAM Rev.* 57 (2015) 483–531.
[15] A.C. Antoulas, *SIAM* 6 (2005).
[16] P.Z. Qian, *J. Am. Stat. Assoc.* 107 (2012) 393–399.
[17] Y.-H. Chang, L. Zhang, X. Wang, S.-T. Yeh, S. Mak, C.-L. Sung, C.F. Jeff Wu, V. Yang, *AIAA J* 57 (2019) 5269–5280.
[18] S. Mak, C.-L. Sung, X. Wang, S.-T. Yeh, Y.-H. Chang, V.R. Joseph, V. Yang, C.F.J. Wu, *J. Am. Stat. Assoc.* 113 (2018) 1443–1456.
[19] S.-T. Yeh, X. Wang, C.-L. Sung, S. Mak, Y.-H. Chang, L. Zhang, C.F.J. Wu, V. Yang, *AIAA J* 56 (2018) 2429–2442.
[20] Y. Huang, V. Yang, *Prog. Energy Combust. Sci.* 35 (2009) 293–364.
[21] V. Yang, *Proc. Combust. Inst.* 28 (2000) 925–942.
[22] X. Wang, H. Huo, Y. Wang, V. Yang, *AIAA J* 55 (2017) 3109–3119.
[23] L. Zhang, X. Wang, Y. Li, S.-T. Yeh, V. Yang, *Phys. Fluids* 30 (2018) 075106.
[24] X. Wang, L. Zhang, Y. Li, S.-T. Yeh, V. Yang, *Combust. Flame* 197 (2018) 204–214.
[25] X. Wang, Y. Wang, V. Yang, *Phys. Fluids* 31 (2019) 065109.